



OPEN

Photocatalytic degradation of methylene blue with spent FCC catalyst loaded with ferric oxide and titanium dioxide

Jiasheng Xu^{1,2}, Te Zhang² & Jie Zhang¹✉

The spent fluid catalytic cracking (FCC) catalyst has been loaded with ferric oxide (Fe_2O_3) and titanium dioxide (TiO_2). Fe-Ti/SF composite (loaded with 5 wt% TiO_2 and 5 wt% Fe_2O_3), Fe/SF composite (loaded with 10 wt% Fe_2O_3) and Ti/SF composite (loaded with 10 wt% TiO_2) have been fabricated via a modified-impregnation method. The band gaps of the Fe-Ti/SF, Fe/SF and Ti/SF composites (evaluated by the energy versus $[F(R_\infty)h\nu]^n$) are 2.23, 1.98 and 3.0 eV, respectively. Electrochemical impedance spectroscopy shows that the Fe-Ti/SF has lower electron transfer resistance, it has the small charge transfer resistance and fast charge transfer rate. The interparticle electrons transfer between the Fe_2O_3 and TiO_2 , which can improve the separation of the photo-electrons and holes. The holes transfer from valence band of TiO_2 to the valence band of Fe_2O_3 , which can provide more active sites around the adsorbed molecules. The methylene blue degradation efficiencies (with the Fe-Ti/SF, Fe/SF and Ti/SF composites) are ~94.2%, ~22.3% and ~54.0% in 120 min, respectively. This work reveals that the spent FCC catalyst as supporter can be loaded with Fe_2O_3 and TiO_2 . This composite is highly suitable for degradation of methylene blue, which can provide a potential method to dispose the spent FCC catalyst in industry.

In the oil refinery, the fluid catalytic cracking (FCC) is an important secondary conversion process^{1–4}. The crude oil can be converted into the valuable small molecules products, which is an essential process for gasoline production⁵. In the FCC process, the catalytic activity of FCC catalyst decreases after several cycles. Metals (V, Ni, and Fe) accumulation occurs via deposition and incorporation into the FCC catalyst body^{6,7}. There are about 840,000 t spent FCC catalyst consumed in the world every year and it is anticipated annual increase of 5%^{8,9}. The spent FCC catalyst are mainly treated via landfill¹⁰. Some researcher explore the coating of spent FCC catalyst as anticorrosive and antimicrobial material, other researcher uses the spent FCC catalyst to recover the precious metal and rare earth, and use spent FCC catalyst as admixtures in mortar and concrete production^{11–13}. Zeolite Y is the main components of the FCC catalyst¹⁴. When the FCC catalyst is deactivated, the pore volume of catalyst is almost intact, which still can be used as a carrier¹⁵.

Titanium dioxide (TiO_2) has been extensively investigated for photocatalytic reaction due to its chemical stability and lack of toxicity^{16–19}. TiO_2 is a wide band gap semiconductor material (3.2 eV)^{20–23}. In photocatalytic reaction, the charge carrier of the TiO_2 is fast recombined, which can be prevented effectively by the heterogeneous structures (with the narrow band gap semiconductor materials)^{24,25}. Fe_2O_3 with narrow band gap (2.2 eV) tends to have short carrier diffusion lengths. Therefore, Fe_2O_3 extends the optical absorption edge to visible light region for TiO_2 . Eskandari et al. and Davari et al. synthesized $\text{TiO}_2/\text{Fe}_2\text{O}_3/\text{zeolite}$ composite, which displayed 89% and 80% photocatalytic degradation efficiency^{26–29}.

In this work, spent FCC catalyst loaded with Fe_2O_3 and TiO_2 was fabricated via a modified-impregnation method. The photocatalytic performance the Fe-Ti/SF, Fe/SF and Ti/SF samples are evaluated by the degradation efficiency of the methylene blue. The recycling experiments of the Fe-Ti/SF composite are implemented by the methylene blue degradation, which evaluates the stability of the Fe-Ti/SF composite. The advantage of

¹College of Chemistry, Chemical Engineering and Environmental Engineering, Liaoning Shihua University, Fushun 113001, People's Republic of China. ²Liaoning Province Key Laboratory for Synthesis and Application of Functional Compounds, College of Chemistry and Chemical Engineering, Bohai University, Jinzhou 121013, People's Republic of China. ✉email: jiezhang@lnpu.edu.cn

this work is that it provides a new way to treat spent FCC catalyst. At present, the spent FCC catalyst are mainly treated by landfill. This method caused severe land pollution and polluted groundwater. The novelty of this work is the introduction spent FCC catalyst as supporter. These composites fabricated via this modified-impregnation method can provide an effective route to dispose the spent FCC catalyst in industry.

Materials and methods

Fabrication of the composites. In a typical experimental procedure, the spent FCC catalyst was loaded with titanium dioxide (5 wt% TiO₂) and ferric oxide (5 wt% Fe₂O₃), it was prepared as follows. 0.85 mL tetrabutyl titanate and 0.31 g ammonium ferric oxalate were dissolved into 4 mL of H₂O₂ solution (~30%). Then 4 g spent FCC catalyst was added into this solution. Finally, this mixture was grinded for 2 h and calcined at 800 °C for 4 h. This sample is denoted as Fe-Ti/SF composite. The other two samples, i.e. Fe/SF composite, the spent FCC catalyst was loaded with ferric oxide (10 wt% Fe₂O₃) and Ti/SF composite, the FCC catalyst was loaded with titanium dioxide (10 wt% TiO₂) were obtained in the above experimental procedure.

Characterizations. The structures of the fabricated composites were tested by power XRD (Rigaku RAD-3C, Cu K α radiation, 10° min⁻¹, 2-*Theta* range 5°–80°). These composites morphology was analyzed by a Scanning Electron Microscope (SEM JEOL S-4800). Fourier transformation infrared (FT-IR) was tested using a spectrometer at a wavenumber covering the range of 400–4,000 cm⁻¹. To measure band gap of these composites, UV-Vis light absorption was recorded on the Diffuse Reflectance spectrophotometer UV-vis. Nitrogen adsorption-desorption tests were executed on a Micrometrics (Tristar 3000) instrument. Transmission electron microscope (TEM, JEOL LED JSM-6700F microscope, Japan) was used to investigate microstructure. Electrochemical impedance spectra (EIS) were tested via using a CHI660D workstation at room temperature. The electrochemical performances of the Fe-Ti/SF, Fe/SF and Ti/SF were analyzed. The working electrode were Fe-Ti/SF, Fe/SF and Ti/SF, respectively. The counter electrode was the Pt plate electrode and reference electrode were the calomel electrode. The electrolyte of the EIS measurements was the Na₂SO₄ aqueous solution (0.2 mol L⁻¹).

Photocatalytic tests. The adsorption and photocatalytic performance of the Fe-Ti/SF, Fe/SF and Ti/SF were tested by photocatalysis degradation of MB. In the experiment, 0.2 g of fabricated composite were added into 200 mL of methylene blue (10 ppm). The photocatalytic tests were driven by irradiation with the 300 W Xenon lamp for 120 min. Before the light irradiation, the reaction system was stirred for 40 min in darkness to ensure the adsorption-desorption equilibrium. The methylene blue was taken at given time interval (20 min). The solutions were centrifuged under 4,000 rpm before analysis.

Results and discussion

Figure 1 shows schematic illustration of the Fe-Ti/SF composite fabrication process. In a typical experimental procedure, 0.85 mL tetrabutyl titanate and 0.31 g ammonium ferric oxalate were dissolved into 4 mL of H₂O₂ solution (~30%). 0.85 mL tetrabutyl titanate and 0.31 g ammonium ferric oxalate were dissolved into 4 mL of H₂O₂ solution (~30%). Then 4 g spent FCC catalyst was added into this solution. Finally, this mixture was grinded for 2 h and calcined at 800 °C for 4 h. The degradation efficiency of methylene blue can be used to evaluate the photocatalytic performance of Fe-Ti/SF composite. The methylene blue can be degraded into the carbon dioxide (CO₂) and water (H₂O) at last.

XRD patterns of the spent FCC catalyst, Fe-Ti/SF, Fe/SF and Ti/SF are shown in Fig. 2 (2-*Theta* range from 5° to 80°). Figure 2a shows XRD patterns of the spent FCC catalyst. There are four diffraction peaks at 6.3°, 10.3°, 12.1° and 15.9°, which can be indexed to (111), (220), (311) and (331) planes of zeolite Y phase (JCPDS No. 77-1551), respectively. Figure 2b,c show the XRD patterns of the Fe/SF and Fe-Ti/SF composite. The intensity of the peak (111) in zeolite Y phase decreases after being loaded Fe₂O₃ or TiO₂. In the range of 12°–25°, the peak intensity is higher than Fig. 2a. In Fig. 2d, there are three peaks at 26.4°, 35.3° and 40.1°. These peaks are corresponded to the (101), (004) and (200) planes of the TiO₂ phase (JCPDS card No. 73-1764), respectively. The size of the loaded TiO₂ is small, which causes the low diffraction peak. Compared with the zeolite Y (111), the diffraction peaks intensity of Fe₂O₃ is lower. Therefore, there no obvious diffraction peaks of Fe₂O₃.

Figure 3 presents scanning electron microscopy (SEM) images of the spent FCC catalyst, Fe/SF, Fe-Ti/SF and Ti/SF samples. In Fig. 3a–c, there are some cracks on the surface. In Fig. 3d, the surface of this composite is covered with Fe₂O₃. In Fig. 3e–f, the peripheral surface of the Fe/SF is coarse. Figure 3g–i show the Fe-Ti/SF composite, this composite is covered with Fe₂O₃ and TiO₂. In Fig. 3i, because the TiO₂ deposits in clusters of irregular shapes, the surface of Fe-Ti/SF composite is rough and jagged. Figure 3j–l show the morphologies of the Ti/SF composite. The TiO₂ particles are loaded on the surface of supporter. As shown in Fig. 3l, the TiO₂ particles with diameter ranging from 50 to 200 nm. There is an aggregation phenomenon between TiO₂. EDS mappings of the Fe-Ti/SF composite are shown in Supplementary Figure S1. It shows the corresponding mappings of Fe-Ti/SF composite, which clearly indicate the homogeneous of Si, O, Al, Fe and Ti elements. The ingredient of zeolite Y are Al₂O₃ and SiO₂. The Al, Si and O elements originate from zeolite Y, the Fe and Ti are loaded on the zeolite Y.

XPS spectra are used to identify the valence states of the elements of the Fe-Ti/SF composite. Supplementary Figure S2 shows the XPS survey spectrum, which suggests the presence of Fe, Ti, Al, Si and O. In Supplementary Figure S2a, the peaks of Fe 2p_{3/2} and Fe 2p_{1/2} are overlap, the three binding energy peaks at 712.0, 721.6 and 725.7 eV. In Supplementary Figure S2b, two banding energy peaks at 458.7 and 464.3 eV correspond to the characteristic of the Ti 2p_{3/2} and Ti 2p_{1/2}. In Supplementary Figure S2c, the peak of Al 2p is overlap, the banding energy peak at 74.6 eV. In Supplementary Figure S2d, the peak of Si 2p is overlap, the banding energy peak at 102.9 eV. In Supplementary Figure S2e, the binding energy peak at 531.8 eV correspond to the characteristic of the O 1 s.

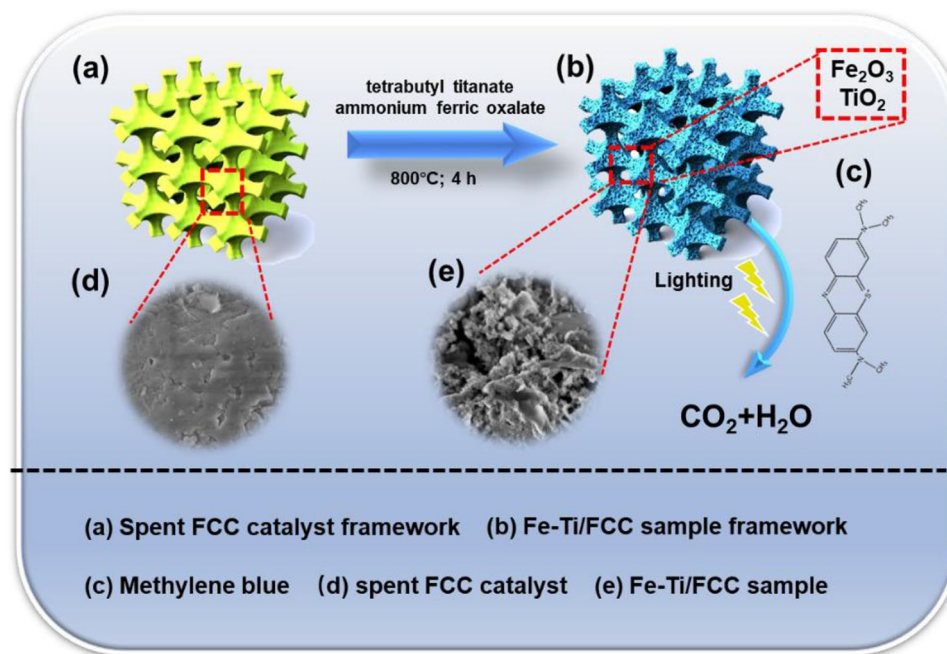


Figure 1. Schematic illustration for the Fe-Ti/SF composites fabricated process. (a) spent FCC catalyst framework, (b) Fe-Ti/SF framework, (c) methylene blue, (d) SEM images of spent FCC catalyst and (e) Fe-Ti/SF.

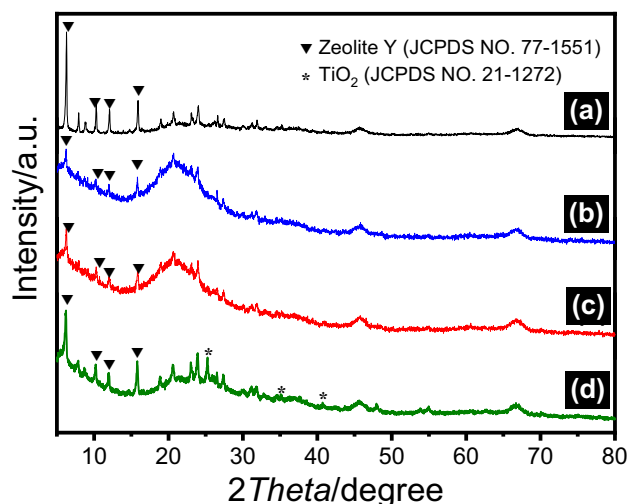


Figure 2. XRD patterns of these samples. (a) spent FCC catalyst, (b) Fe/SF, (c) Fe-Ti/SF and (d) Ti/SF.

Figure 4 shows the TEM images of the Fe-Ti/SF composite. In Fig. 4a–c, the Fe_2O_3 and TiO_2 particles are attached to the surface of the spent FCC catalyst. The crystallography of the Fe-Ti/SF composite is investigated with high-resolution TEM (HRTEM). In the Fig. 4d, the nanostructured heterojunction is formed between Fe_2O_3 and TiO_2 . The intimately contacted interface is important for accelerating the separation of the electrons and holes. The HRTEM image in Fig. 4d shows two kinds of lattice fringes, the interplanar crystal spacing of 0.352 and 0.252 nm are corresponded TiO_2 (101) and Fe_2O_3 (110), respectively. More TEM images of the Fe-Ti/SF composite are shown in Supplementary Figure S3a–c. The dark color regions under TEM indicate thickness of the zeolite Y. The TEM images further show that Fe_2O_3 and TiO_2 are loaded on the surface of supporter.

In Fig. 5, the macropores properties of the spent FCC catalyst, Fe/SF, Fe-Ti/SF and Ti/SF are analyzed. These insets show the pore diameter of these samples. All the samples show the type-II isotherms, which are corresponded of macropores materials (IUPAC classification). The isotherms of these samples exhibit H3 hysteresis loops associated with the presence of macropores. The pore diameter of the spent FCC catalyst, Fe/SF, Fe-Ti/SF and Ti/SF are 5.6, 5.8, 5.9 and 5.8 nm, respectively. It shows that these samples are macroporous. The surface

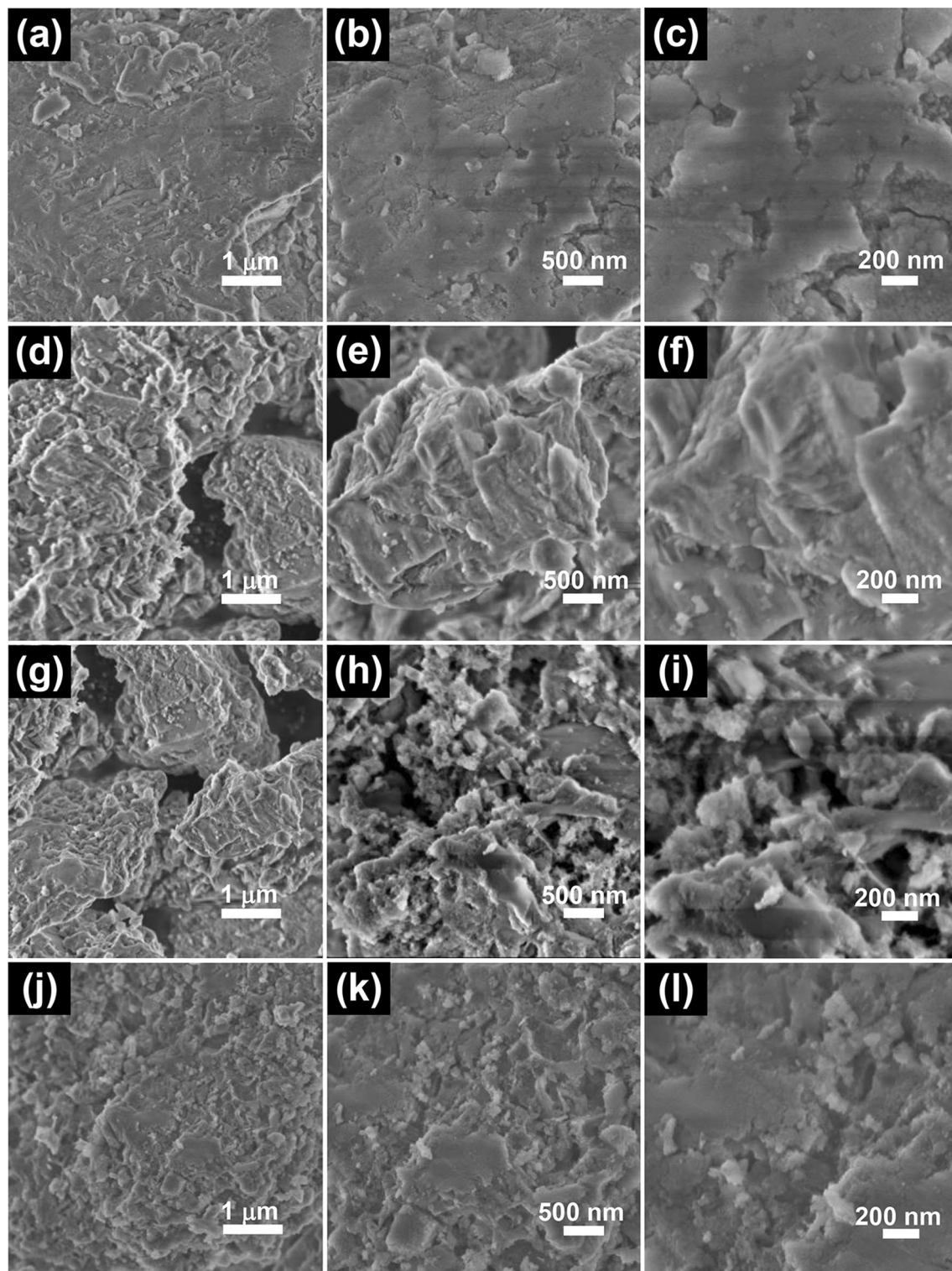


Figure 3. SEM images of the spent FCC catalyst, Fe-Ti/SF, Fe/SF and Ti/SF samples with different morphologies. (a–c) spent FCC, (d–f) Fe-Ti/SF, (g–i) Fe/SF, (j–l) Ti/SF.

areas of these composites (spent FCC catalyst, Fe/SF, Fe-Ti/SF and Ti/SF) are calculated to be 226.3, 253.7, 264.5 and 235.2 $\text{m}^2 \text{g}^{-1}$, respectively. Due to the large surface area, these samples can absorb more methylene blue.

As shown in Supplementary Figure S4, the UV-Vis absorbance spectra of the Fe-Ti/SF, Fe/SF and Ti/SF composites were evaluated. The adsorption edges of the Fe-Ti/SF, Fe/SF and Ti/SF composites are 510, 540 and 400 nm, respectively. The Kubelka–Munk function is applied to determine the band gaps of Fe-Ti/SF, Fe/SF and Ti/SF composites. As shown in inset of the Supplementary Figure S2, the band gaps of the Fe-Ti/SF, Fe/SF and Ti/SF composites from the energy versus $[F(R_\infty)/h\nu]^n$ can be estimated. R_∞ and $F(R_\infty)$ are the limiting

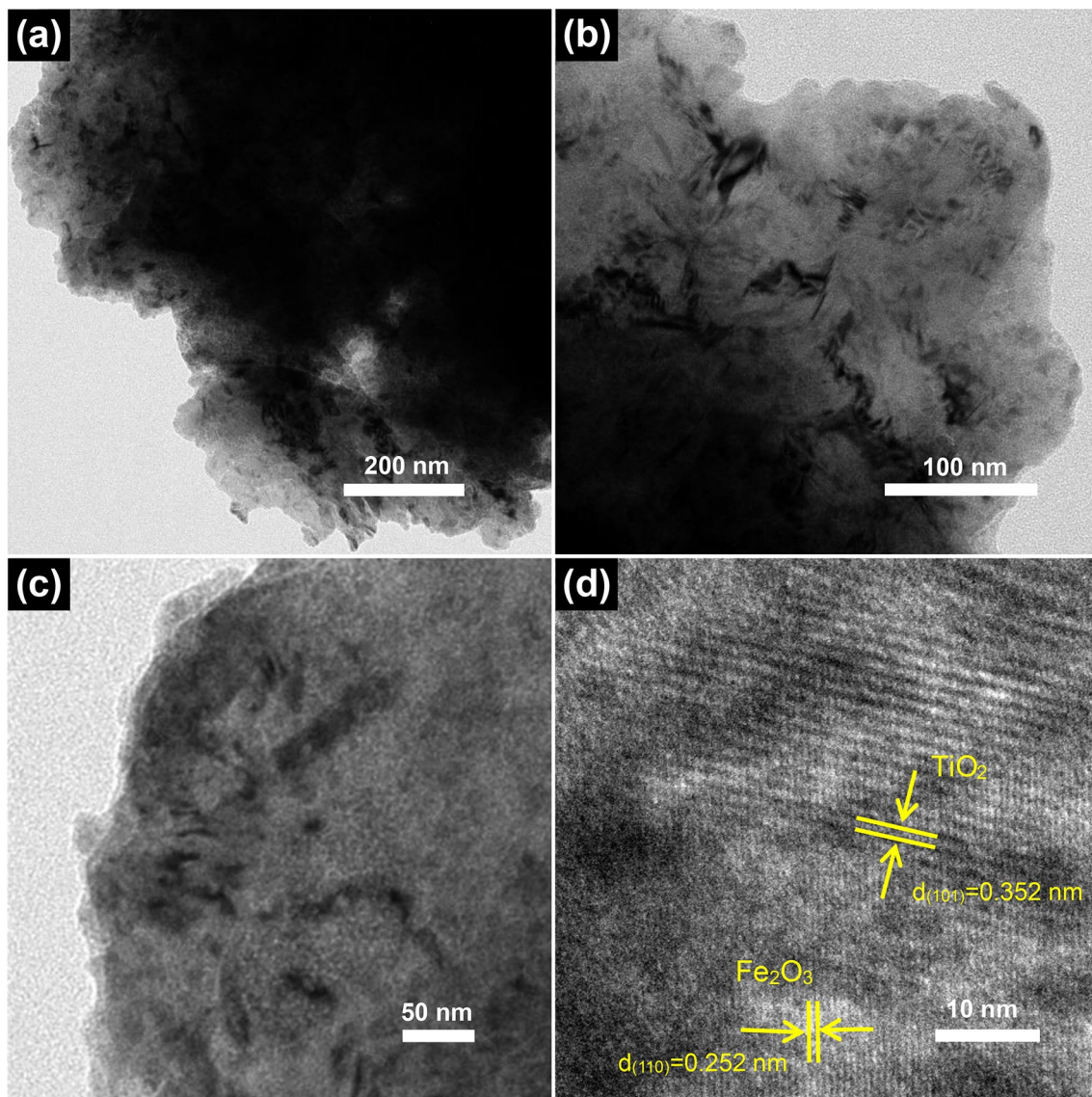


Figure 4. (a–c) TEM images of the Fe-Ti/SF, (d) HRTEM images of the Fe-Ti/SF.

reflectance and Kubelka–Munk function, respectively. The slope of the Tauc plot fit well at $n = 1/2$, which indicated an indirect transition. The band gaps of the Fe-Ti/SF, Fe/SF and Ti/SF composites are 2.23, 1.98 and 3.0 eV, respectively^{30,31}. The partial absorption in the visible range is determined by the band gap energy value, which shows that these samples have potential photocatalytic activity.

The schematic diagram of the band position of Fe-Ti/SF is shown in Fig. 6. The interparticle electrons intensity of Fe-Ti/SF is higher than the single component Fe₂O₃ or TiO₂, which can promote the separation of electrons and holes. The Fermi levels of the Fe₂O₃ and TiO₂ are lower than their conduction band (CB). In the heterostructure, the Fermi levels of Fe₂O₃ and TiO₂ reach a new equalization state. There is a new electric field between the Fe₂O₃ and TiO₂. The interparticle electrons rapidly transfer in the heterostructure between the Fe₂O₃ and TiO₂. The electrons of a higher CB transfer to the lower one, the holes move in the opposite way. The electrons of Fe₂O₃ (CB) transfer to TiO₂ (CB). The holes of TiO₂ (VB) transfer to Fe₂O₃ (VB). The electrons are trapped by O₂ (dissolved in the methylene blue) to form [•]O₂, the [•]O₂ oxidized the methylene blue. Finally, the methylene blue is degraded in CO₂ and H₂O.

The electron transfer efficiency can be measured by the electrochemical impedance spectroscopy (EIS). As shown in Fig. 7, the radius (Nyquist plot) of the Fe-Ti/SF is much smaller than those of Fe/SF and Ti/SF, which shows that Fe-Ti/SF has lower electron transfer resistance. The heterostructure of the Fe₂O₃ and TiO₂ enhances the separation of the electrons and holes.

In Fig. 8, the Fourier transform infrared spectroscopy (FT-IR) spectra of the spent FCC catalyst, Fe/SF, Fe-Ti/SF and Ti/SF are measured. The peak at 3,425 cm⁻¹ corresponds to the absorption of the stretching vibration of O–H group stretching. The peak at 1645 cm⁻¹ corresponds to the bending vibration absorption of the O–H³². In Fig. 8a–d, the peak at 1,082 cm⁻¹, 848 cm⁻¹ and 456 cm⁻¹ correspond to the stretching or bending vibration of the Si–O–Si^{33,34}. In the samples of the (b) Fe/SF and (c) Fe-Ti/SF, the absorption peaks at 560, 610, 1,100, and

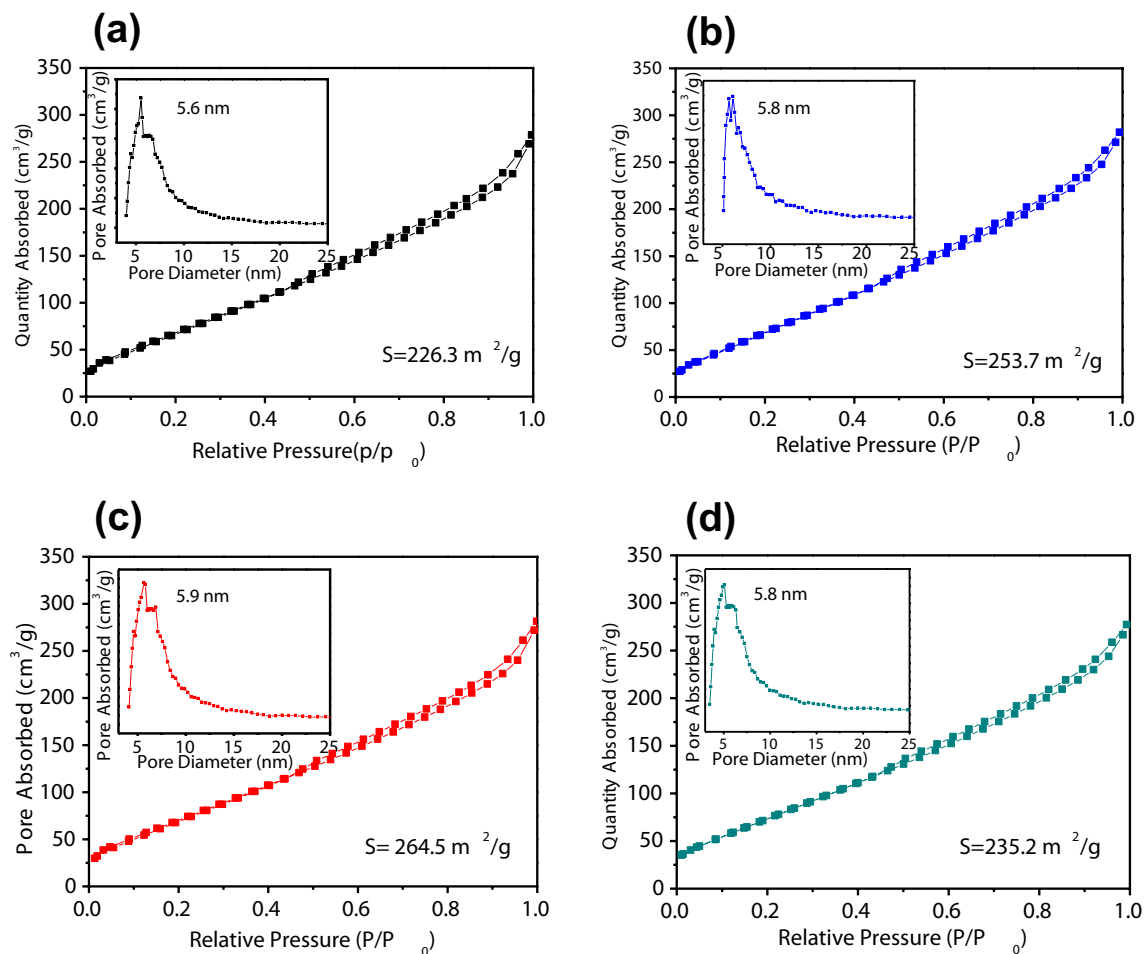


Figure 5. Brunauer–Emmett–Teller (BET) nitrogen adsorption and desorption isotherms of (a) spent FCC catalyst, (b) Fe/SF, (c) Fe-Ti/SF and (d) Ti/SF. The corresponding pore size distribution curves are illustrated in the inset.

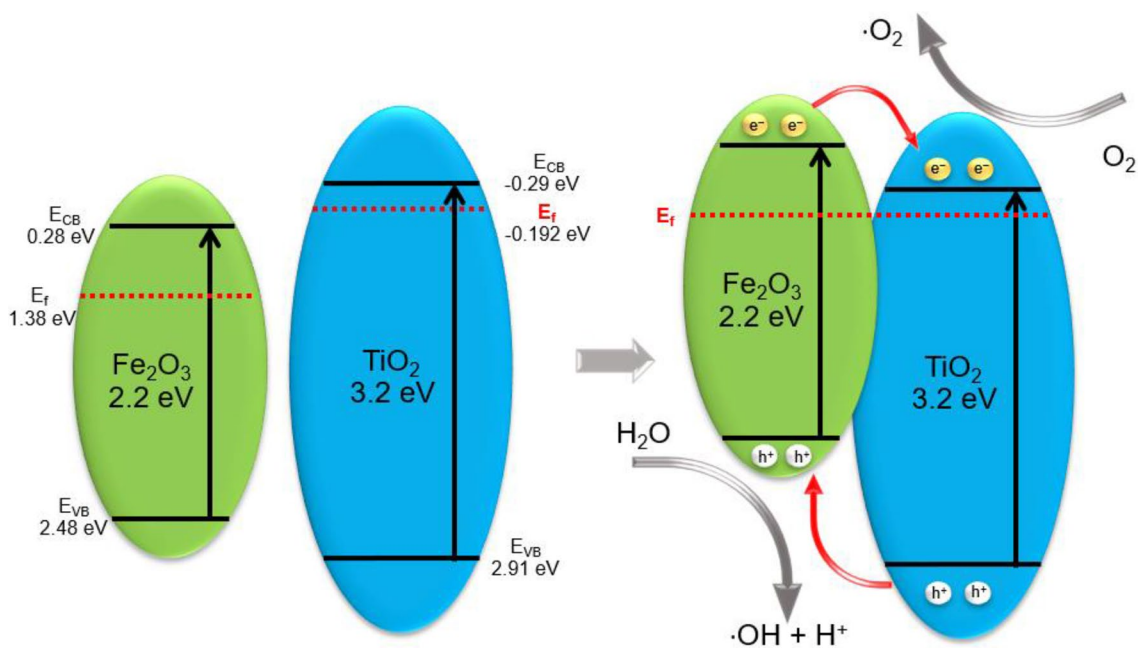


Figure 6. Schematic diagram of the band position of Fe-Ti/SF.

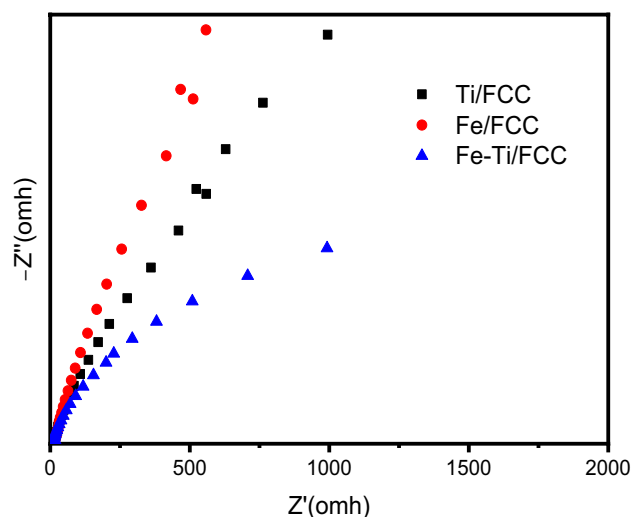


Figure 7. Electrochemical impedance spectroscopy (EIS) analysis of Fe-Ti/SF, Fe/SF and Ti/SF.

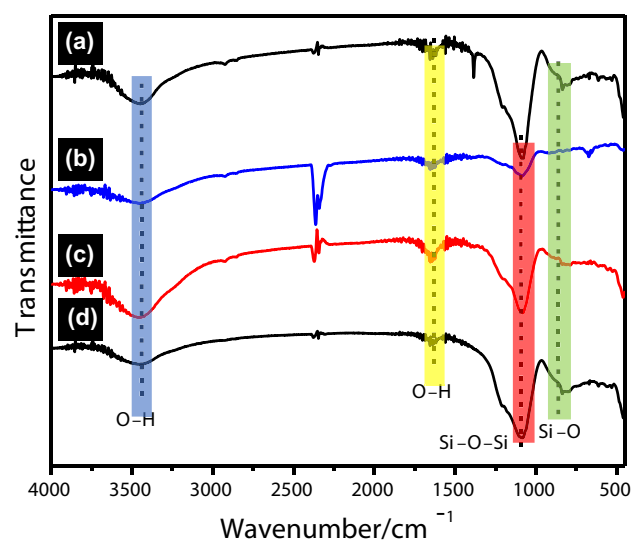


Figure 8. FT-IR spectra of (a) spent FCC catalyst, (b) Fe/SF, (c) Fe-Ti/SF and (d) Ti/SF, respectively.

$3,500\text{ cm}^{-1}$ correspond to the stretching vibration of Fe-O. In Fig. 8d, the peaks at 910 cm^{-1} to 960 cm^{-1} corresponds to the stretching vibration of the Ti-O-Si.

In Fig. 9, the photocatalytic performance of the Fe-Ti/SF is evaluated by the methylene blue degradation experiment. With increase of the reaction time, the methylene blue characteristic peak is gradually declined, which indicates concentration of methylene blue is gradually declined. The photocatalytic degradation efficiency of the methylene blue is $\sim 94.2\%$. The inset of Fig. 9 shows the color change of the methylene blue. Figure. S5 shows the degradation of methylene blue with the Fe-Ti/SF, Fe/SF and Ti/SF composites. The methylene blue degradation efficiencies (with Fe-Ti/SF, Fe/SF and Ti/SF composites) are $\sim 94.2\%$, $\sim 22.3\%$ and $\sim 54.0\%$ in 120 min, respectively. The results show that the Fe-Ti/SF composite has the highest photocatalytic activity. Supplementary Figure S6 shows the photocatalytic degradation efficiency of methylene blue with Fe-Ti/SF, $\text{Fe}_2\text{O}_3\text{-TiO}_2$, Fe_2O_3 and TiO_2 .

As shown in Fig. 10, the recycling experiments of the Fe-Ti/SF composite are implemented by the methylene blue degradation, which evaluates the stability of this Fe-Ti/SF composite. After the fourth cycle reaction, the photocatalytic activity of the Fe-Ti/SF composite is not significant loss. The degradation efficiency of the methylene blue with Fe-Ti/SF composite decreases to 84.0% from the pristine degradation efficiency (94.2%). These results indicate that the Fe-Ti/SF exhibit a relatively stable photocatalytic performance.

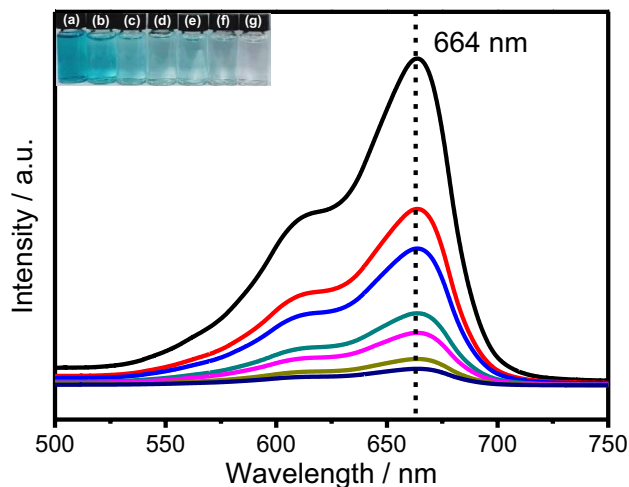


Figure 9. UV-Vis adsorption spectra of degradation of methylene blue with Fe-Ti/SF composite. Inset shows the photographs of methylene blue solution. The inset shows the photographs of methylene blue solution: the 0 min, 20 min, 40 min, 60 min, 80 min, 100 min and 120 min, which corresponds with (a–g), respectively.

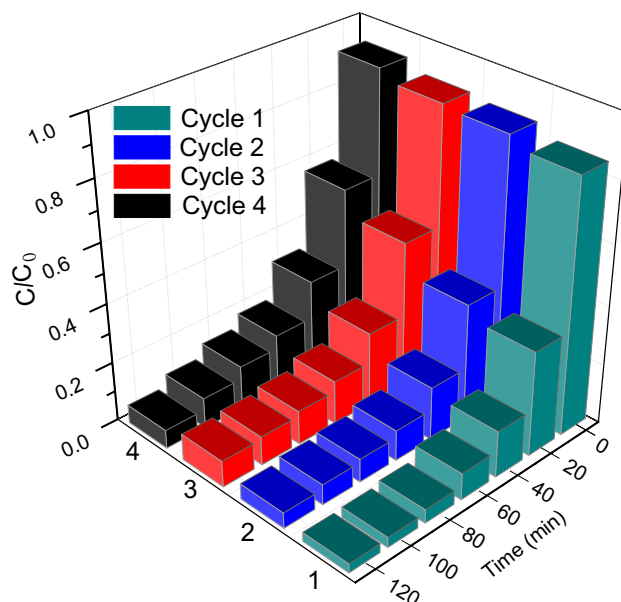


Figure 10. Recycling experiments of photocatalytic reduction of methylene blue with Fe-Ti/SF.

Conclusion

In summary, the Fe-Ti/SF, Fe/SF and Ti/SF composites have been successfully fabricated via a modified-impregnation method. The adsorption and degradation tests were carried out for 120 min to evaluate Fe-Ti/SF, Fe/SF and Ti/SF photocatalytic performance, the methylene blue degradation efficiencies are ~94.2%, ~22.3% and ~54.0%, respectively. The interparticle electrons rapidly transfer in the heterostructure between the Fe_2O_3 and TiO_2 . The radius (Nyquist plot) of the Fe-Ti/SF is much smaller than those of Fe/SF and Ti/SF, which shows Fe-Ti/SF has lower electron transfer resistance and fast charge transfer rate. After the fourth cycle reaction, the photocatalytic activity of the Fe-Ti/SF composite reduces 10.2% (the photocatalytic degradation efficiency of methylene blue is from 94.2 to 84.0%). The spent FCC catalyst loaded with Fe_2O_3 and TiO_2 has stable photocatalytic performance. This modified-impregnation method, the spent FCC catalyst is used as the photocatalyst supports, which provides a potential method to dispose the spent FCC catalyst in the areas of environment protection.

Received: 30 March 2020; Accepted: 16 July 2020

Published online: 29 July 2020

References

- Shi, J. *et al.* Nitrogen chemistry and coke transformation of FCC coked catalyst during the regeneration process. *Sci. Rep.* **6**, 27309 (2016).
- Ferella, F. *et al.* Synthesis of zeolites from spent fluid catalytic cracking catalyst. *J. Clean. Prod.* **230**, 910–926 (2019).
- Vogt, E. T. C. & Weckhuysen, B. M. Fluid catalytic cracking: Recent developments on the grand old lady of zeolite catalysis. *Chem. Soc. Rev.* **44**, 7342–7370 (2015).
- Yuan, L. *et al.* Adsorption and mechanistic study for phosphate removal by magnetic Fe₃O₄-doped spent FCC catalysts adsorbent. *Chemosphere* **219**, 183–190 (2019).
- Chen, X. *et al.* Synthesis, characterization and activity performance of nickel-loaded spent FCC catalyst for pine gum hydrogenation. *RSC Adv.* **9**, 6515–6525 (2019).
- Le, T., Wang, Q., Ravindra, A. V., Li, X. & Ju, S. Microwave intensified synthesis of zeolite-Y from spent FCC catalyst after acid activation. *J. Alloys Compd.* **776**, 437–446 (2019).
- Wu, L., Khalil, F., Smith, G. M., Yilmaz, B. & McGuire, R. Effect of solvent on the impregnation of contaminant nickel for laboratory deactivation of FCC catalysts. *Micropor. Mesopor. Mat.* **207**, 195–199 (2015).
- Chen, C. M., Yu, J., Yoza, B. A., Li, Q. X. & Wang, G. A novel “wastes-treat-wastes” technology: Role and potential of spent fluid catalytic cracking catalyst assisted ozonation of petrochemical wastewater. *J. Environ. Manag.* **152**, 58–65 (2015).
- Akcil, A., Vegliò, F., Ferella, F., Okudan, M. D. & Tuncuk, A. A review of metal recovery from spent petroleum catalysts and ash. *Waste Manag.* **45**, 420–433 (2015).
- Su, B., Shi, L., Liu, N., Wang, X. & Meng, X. Removal of sulfur compounds from LPG by heteropoly acid-modified spent FCC catalyst. *Appl. Organomet. Chem.* **33**, 1–7 (2019).
- Trivedi, P. A., Solanki, N. M., Butani, N. & Parikh, P. A. Investigation on corrosion control of mild steel buried in soil by spent FCC catalyst coating. *J. Ind. Eng. Chem.* **20**, 2264–2271 (2014).
- Le-Phuc, N. *et al.* Towards efficient extraction of La(III) from spent FCC catalysts by alkaline pre-treatment. *Miner. Eng.* **127**, 1–5 (2018).
- Neves, R., Vicente, C., Castela, A. & Montemor, M. F. Durability performance of concrete incorporating spent fluid cracking catalyst. *Cement. Concret. Comp.* **55**, 308–314 (2015).
- Scherzer, J. Octane-enhancing, zeolitic FCC catalysts: Scientific and technical aspects. *Catal. Rev.* **31**, 215–354 (1989).
- Trivedi, P. A., Parmar, P. R. & Parikh, P. A. Spent FCC catalyst: Potential anti-corrosive and anti-biofouling material. *J. Ind. Eng. Chem.* **20**, 1388–1396 (2014).
- Wang, T. *et al.* Preparation of ordered TiO₂ nanofibers/nanotubes by magnetic field assisted electrospinning and the study of their photocatalytic properties. *Ceram. Int.* **45**, 14404–14410 (2019).
- Mohammadi, M., Rezaee Roknabadi, M., Behdani, M. & Kompany, A. Enhancement of visible and UV light photocatalytic activity of rGO-TiO₂ nanocomposites: The effect of TiO₂/graphene oxide weight ratio. *Ceram. Int.* **45**, 12625–12634 (2019).
- Zhao, Y. *et al.* Tuning oxygen vacancies in ultrathin TiO₂ nanosheets to boost photocatalytic nitrogen fixation up to 700 nm. *Adv. Mater.* **31**, 1–9 (2019).
- Li, X., Qian, J. H., Xu, J. S. & Xing, J. J. E. T. Synthesis, characterization and electrical properties of TiO₂ modified with SiO₂ and antimony-doped tin oxide. *J. Mater. Sci. Mater. Electron.* **29**, 12100–12108 (2018).
- Wang, W. *et al.* Edge-enriched ultrathin MoS₂ embedded yolk-shell TiO₂ with boosted charge transfer for superior photocatalytic H₂ evolution. *Adv. Funct. Mater.* **29**, 1–10 (2019).
- Low, J., Dai, B., Tong, T., Jiang, C. & Yu, J. In situ irradiated X-ray photoelectron spectroscopy investigation on a direct Z-scheme TiO₂/CdS composite film photocatalyst. *Adv. Mater.* **31**, 1–5 (2019).
- Shirai, K. *et al.* Water-assisted hole trapping at the highly curved surface of nano-TiO₂ photocatalyst. *J. Am. Chem. Soc.* **140**, 1415–1422 (2018).
- Chen, Q., Zhou, M., Zhang, Z. M., Tang, T. & Wang, T. Preparation of TiO₂ nanotubes/reduced graphene oxide binary nanocomposites enhanced photocatalytic properties. *J. Mater. Sci. Mater. Electron.* **28**, 9416–9422 (2017).
- Perveen, S. & Farrukh, M. A. Influence of lanthanum precursors on the heterogeneous La/SnO₂-TiO₂ nanocatalyst with enhanced catalytic activity under visible light. *J. Mater. Sci. Mater. Electron.* **28**, 10806–10818 (2017).
- Ilkhechi, N. N., Ghobadi, N. & Akbarpour, M. R. Enhanced optical and photo catalytic properties of V and La co doped TiO₂ nanoparticles. *J. Mater. Sci. Mater. Electron.* **28**, 6426–6434 (2017).
- de Krafft, K. E., Wang, C. & Lin, W. Metal-organic framework templated synthesis of Fe₂O₃/TiO₂ nanocomposite for hydrogen production. *Adv. Mater. Res.* **24**, 2014–2018 (2012).
- Silvestri, S. & Foletto, E. L. Preparation and characterization of Fe₂O₃/TiO₂/clay plates and their use as photocatalysts. *Ceram. Int.* **43**, 14057–14062 (2017).
- Davari, N., Farhadian, M., Nazar, A. R. S. & Homayonfal, M. Degradation of diphenhydramine by the photocatalysts of ZnO/Fe₂O₃ and TiO₂/Fe₂O₃ based on clinoptilolite: Structural and operational comparison. *J. Environ. Chem. Eng.* **5**, 5707–5720 (2017).
- Eskandari, P., Farhadian, M., Solaimany Nazar, A. R. & Jeon, B.-H. Adsorption and photodegradation efficiency of TiO₂/Fe₂O₃/PAC and TiO₂/Fe₂O₃/zeolite nanophotocatalysts for the removal of cyanide. *Ind. Eng. Chem. Res.* **58**, 2099–2112 (2019).
- Xu, J. S., Pan, C. S., Takata, T. & Domen, K. Photocatalytic overall water splitting on the perovskite-type transition metal oxynitride CaTaO₂N under visible light irradiation. *Chem. Commun.* **51**, 7191–7194 (2015).
- Zhang, H. D. *et al.* Microwave-assisted synthesis of Cu₂O microcrystals with systematic shape evolution from octahedral to cubic and their comparative photocatalytic activities. *RSC Adv.* **4**, 38059–38063 (2014).
- Yosefi, L. & Haghghi, M. Fabrication of nanostructured flowerlike p-BiOI/p-NiO heterostructure and its efficient photocatalytic performance in water treatment under visible-light irradiation. *Appl. Catal. B Environ.* **220**, 367–378 (2018).
- Król, M., Minkiewicz, J. & Mozgawa, W. IR spectroscopy studies of zeolites in geopolymeric materials derived from kaolinite. *J. Mol. Struct.* **1126**, 200–206 (2016).
- Tang, R., Chen, T., Chen, Y., Zhang, Y. & Wang, G. Core-shell TiO₂@SiO₂ catalyst for transesterification of dimethyl carbonate and phenol to diphenyl carbonate. *Chin. J. Catal.* **35**, 457–461 (2014).

Acknowledgements

This work was supported by the Talent Scientific Research Fund of LSHU (#2020XJL-001) and the National Key R&D Program of China (#2018YFF0215200).

Author contributions

J.X. conceived the idea and designed the experiments. T.Z. collected and analyzed the data and wrote the main manuscript. J.Z. contributed substantially to revisions and supervised paper. All authors reviewed the manuscript.

Competing interests

The authors declare no competing interests.

Additional information

Supplementary information is available for this paper at <https://doi.org/10.1038/s41598-020-69643-2>.

Correspondence and requests for materials should be addressed to J.Z.

Reprints and permissions information is available at www.nature.com/reprints.

Publisher's note Springer Nature remains neutral with regard to jurisdictional claims in published maps and institutional affiliations.



Open Access This article is licensed under a Creative Commons Attribution 4.0 International License, which permits use, sharing, adaptation, distribution and reproduction in any medium or format, as long as you give appropriate credit to the original author(s) and the source, provide a link to the Creative Commons license, and indicate if changes were made. The images or other third party material in this article are included in the article's Creative Commons license, unless indicated otherwise in a credit line to the material. If material is not included in the article's Creative Commons license and your intended use is not permitted by statutory regulation or exceeds the permitted use, you will need to obtain permission directly from the copyright holder. To view a copy of this license, visit <http://creativecommons.org/licenses/by/4.0/>.

© The Author(s) 2020